

Ultrasensitive Multiparameter Phenotyping of Rare Cells Using an Integrated Digital-Molecular-Counting Microfluidic Well Plate

Shiuan-Haur Su, Yujing Song, Michael W. Newstead, Tao Cai, MengXi Wu, Andrew Stephens, Benjamin H. Singer,* and Katsuo Kurabayashi*

Integrated microfluidic cellular phenotyping platforms provide a promising means of studying a variety of inflammatory diseases mediated by cell-secreted cytokines. However, immunosensors integrated in previous microfluidic platforms lack the sensitivity to detect small signals in the cellular secretion of proinflammatory cytokines with high precision. This limitation prohibits researchers from studying cells secreting cytokines at low abundance or existing at a small population. Herein, the authors present an integrated platform named the “digital Phenoplate (dPP),” which integrates digital immunosensors into a microfluidic chip with on-chip cell assay chambers, and demonstrates ultrasensitive cellular cytokine secretory profile measurement. The integrated sensors yield a limit of detection as small as 0.25 pg mL^{-1} for mouse tumor necrosis factor alpha (TNF- α). Each on-chip cell assay chamber confines cells whose population ranges from ≈ 20 to 600 in arrayed single-cell trapping microwells. Together, these microfluidic features of the dPP simultaneously permit precise counting and image-based cytometry of individual cells while performing parallel measurements of TNF- α released from rare cells under multiple stimulant conditions for multiple samples. The dPP platform is broadly applicable to the characterization of cellular phenotypes demanding high precision and high throughput.

1. Introduction

Cytokines are small pleiotropic cell-signaling proteins with the functions including promoting phagocytosis, recruiting immune cells, and regulating inflammation.^[1,2] Deciphering cellular cytokine secretion facilitates obtaining the full picture of the mechanisms of inflammatory diseases involving complicated interactions of immune cells in vivo, such as sepsis,^[3–5] graft versus host disease,^[6,7] and Alzheimer’s disease (AD).^[8–10] Cytokine release assays are one of the primary methods to quantify the functional cytokines secreted from cells ex vivo. However, the current gold standard of conventional cell culture and analysis of supernatants by enzyme-linked immunosorbent assay (ELISA), typically requires either large cell populations or highly secreting cells to produce assayable cytokine concentrations,^[11] resulting in a limited ability to interrogate low-level cytokine secreting cell types,^[12,13] rare cells,^[14,15] or low-abundant, yet critical bio-

markers. Intracellular cytokine staining and single cell secretion microfluidic platforms^[16–20] provide data on immunophenotypic heterogeneity at single-cell resolution. While these analyses excel at revealing the heterogeneity within cell populations,^[21] analyses of multiple patients or animals required to robustly understand responses to inherently noisy disease states, experimental manipulations, and treatment responses remain impractical. Additionally, these single-cell phenotyping methods are only feasible by extreme volume confinement of cells to amplify the analyte concentration to the detectable range. The volume confinement may cause phenotypic change/loss to cells due to endogenous signaling^[22–24] and alter the assay outcomes. Discrepancies between single cell assays and the gold standard have also been reported when attempting to pool single cell data to reconstruct bulk results possibly caused by the loss of paracrine signaling and enhanced autocrine feedbacks in single cell secretion assays.^[25] There is thus still immense value in understanding population-level dynamics of immunologically active cells in inflammatory conditions.


Multiple cells separation technologies, including density gradient centrifugation, fluorescent-activated cell sorting, magnetic

S.-H. Su, Y. Song, T. Cai, M. Wu, A. Stephens, Prof. K. Kurabayashi
Department of Mechanical Engineering
University of Michigan
Ann Arbor, MI 48109, USA
E-mail: katsuo@umich.edu

M. W. Newstead, Prof. B. H. Singer
Department of Internal Medicine
Division of Pulmonary and Critical Care Medicine
University of Michigan
Ann Arbor, MI 48109, USA
E-mail: singerb@med.umich.edu

Prof. B. H. Singer, Prof. K. Kurabayashi
Michigan Center for Integrative Research in Critical Care
University of Michigan
Ann Arbor, MI 48109, USA

Prof. K. Kurabayashi
Department of Electrical Engineering and Computer Science
University of Michigan
Ann Arbor, MI 48109, USA

 The ORCID identification number(s) for the author(s) of this article can be found under <https://doi.org/10.1002/sml.202101743>.

DOI: 10.1002/sml.202101743

bead separation, and buoyancy bead separation allow for the purification of specific cell populations from complex mixtures derived from blood, body fluids, and tissues.^[26] In many conditions, however, only small numbers of primary cells can be isolated. Cell number may be limited by low cell abundance, as in cerebrospinal fluid in neuroinflammatory conditions,^[27,28] by limited sample volume, such as in serial blood samples or bronchoalveolar lavage from murine disease models,^[29] or by the difficulty of isolating live cells from tissue, as when isolating immune cells from brain tissue.^[30] The difficulty of assaying cell secretion *ex vivo* is compounded by the need to study the responses of small number of cells to multiple conditions, further dividing the number of cells available per assay if robust and reproducible conclusions are to be reached. Integrated microfluidic cellular secretory platforms monitoring collective cell cytokine secretion response have been widely explored to realize higher measurement throughput,^[31,32] lower cell and reagent usage per measurement^[31–40] and increased assay speed.^[34–37,40] These microfluidic platforms incorporate microscale immunosensors based on localized surface plasmon resonance,^[35,36,40] mechanically induced trapping of molecular interactions,^[32] bead-based amplified luminescent proximity homogeneous assay^[34,37] or antibody arrays.^[31,33,38,39] Despite their integrability in a microfluidic platform, these immunosensors still suffer from limited sensitivity which still prevents the microfluidic analysis from tackling the challenges in rare cell clinical studies as presented above.

Herein, we propose an ultrasensitive multiparameter cellular phenotyping method employing digital molecular counting immunosensors^[41–43] integrated into a microfluidic platform named the “digital Phenoplate (dPP).” The dPP enables analyzing cellular phenotypes associated with cytokine secretion and other cellular functions (e.g., phagocytic activity and cell death) that can be simultaneously observed by digital protein immunosensing and on-chip image-based cytometry. The integrated digital immunosensors preserve analyte concentration-signal linearity even at a sub-pg mL⁻¹ level and achieve a limit of detection of 0.25 pg mL⁻¹ for mouse tumor necrosis factor alpha (TNF- α), which allows for testing fewer than 20 cells per assay. The dPP chip has 48 on-chip assay chambers, each containing 22 400 single-cell-trapping microwells and a digital immunosensor pattern (Figure 1A). The spatially patterned arrangement of the microwell and digital sensor arrays permits ultrasensitive quantification of cytokine molecules released from a precisely counted number of cells in distinct locations on the dPP chip. This device feature enables us to estimate the lower cell assay number bound to profile the collective cell cytokine secretion with consistent data. Above this threshold, normalization to the amount of secreted cytokines per cell (fg cell⁻¹) is validated as a representative metric to the cell phenotype and nearly independent of the assayed cell number.

Using the dPP, we demonstrate simultaneous characterization of the cytokine secretory behavior and amyloid beta (A β) phagocytic activity of low-abundant primary microglia isolated from \approx 1-year-old mice which over-express A β .^[44] Taking the animal-to-animal variability into account, our data analysis unveils the subtle functional phenotypic differences in microglia between aged Alzheimer’s disease model (5xFAD) and wild-type mice. Our test shows that the TNF- α secretion of microglia

is elevated in mice with 5xFAD genotype. Additionally, both 5xFAD and wild-type mice are observed to actively secrete TNF- α upon acute A β exposure *ex vivo*. The dPP’s ability to perform precise, reproducible measurements of microglial activity with the small population under multiple conditions and replicates provides remarkable advantages. These advantages are to facilitate robust and rigorous animal or clinical studies targeting host heterogeneity defined by cellular phenotypes.

2. Results and Discussion

2.1. Digital Phenoplate Platform for Cellular Phenotyping and Imaging

The dPP platform comprises 1) a thin polydimethylsiloxane (PDMS) film (300 μ m) bonded on a glass substrate (“microwell layer”), which has a cell trapping/culture region with microwell arrays (“cell array patch”) and a digital sensor region with smaller bead trapping microwell arrays (“digital sensor array patch”), and 2) a PDMS layer ($h = 80 \mu$ m) with cell and bead patterning channels (“Channel Layer 1”) or one with channels for cell-digital sensor coupling (“Channel Layer 2”) (Figure 1A). The features on all of those PDMS layers were fabricated using conventional soft lithography and SU-8 molding (see Experimental Section for details). The microwell layer allows us to seamlessly integrate the target cell trapping process ($d = 16 \mu$ m, $h = 20 \mu$ m, 22 400 wells per array) with the bead-based digital immunoassay ($d = 3.4 \mu$ m, $h = 3.8 \mu$ m, 66 724 sensor wells per array).

The on-chip cellular phenotyping assay procedure starts with manually applying pressure to Channel Layer 1 onto the microwell layer, which temporarily seals its top through intrinsic adherence force between PDMS materials. Subsequently, anti-hamster IgG secondary antibody-coated beads are settled into the digital sensor microwells and later blocked using the sensor patterning channels on the Channel Layer 1. Target cells prepared into single-cell suspensions (see Experimental Section and Figure S1 (Supporting Information) for details in RAW 264.7 and primary microglia cell preparation; Figure S2 (Supporting Information) for microglia isolation purity) are then loaded onto and trapped in the cell trapping microwells via the cell patterning channels (Figure 1B (i)). Excess or untrapped cells are then washed away with a culture media solution. All cells are securely trapped in the designated microwell sites. For stickier adherent cell applications, the dPP can be precoated with Pluronic to prevent undesired cell adhesion. With the current channel design, up to 8 different cell samples can be seeded on a single dPP chip, and each sample can be tested with up to 6 different stimulation conditions or 6 assay replicates in parallel.

After trapping the cells, the medium is pulled out from the cell patterning and bead patterning channels with a pipette, and then the Channel Layer 1 is peeled off and replaced with the Channel Layer 2. Here, the Channel Layer 2 provides a fluidic connection between each cell array patch with its neighboring digital sensor array patch. The resulting dPP chip yields 48 assay chambers, each containing a cell array/digital sensor array patch pair, and 8 digital sensor array

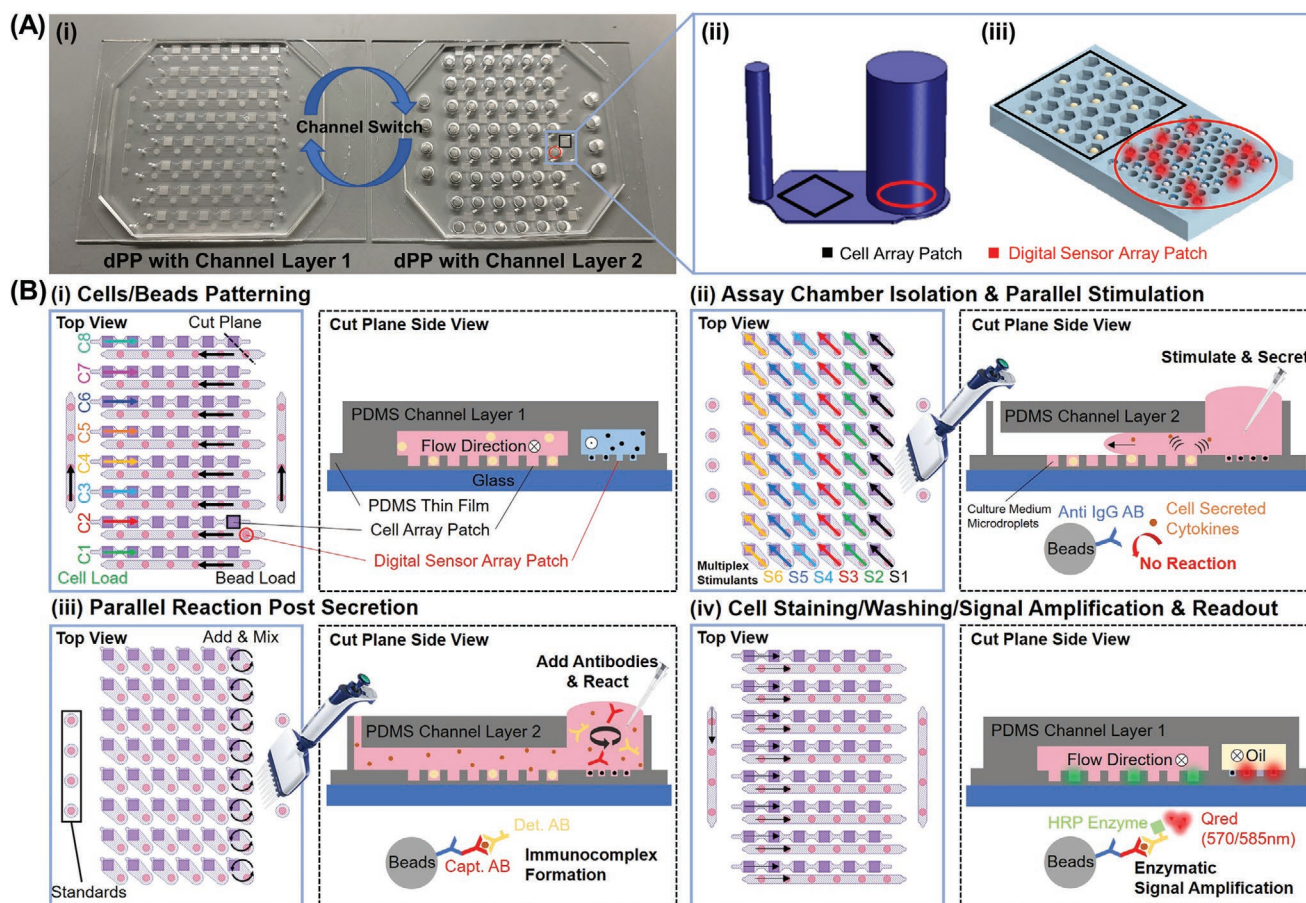


Figure 1. Ultrasensitive multiparameter cellular phenotyping platform: digital Phenoplate (dPP). A) (i) Photoimage of two dPP chips with 2 types of microfluidic channels. The platform comprises a thin PDMS film with cell/bead trapping microwells, which is bonded on top of a glass substrate and two interchangeable PDMS Channel Layers. The dPP chip can accommodate up to 8 different samples with 6 stimulation conditions per sample (48 measurements per chip). (ii) 3D schematic of a microfluidic assay chamber on Channel Layer 2. The marked black and red regions indicate the positions of the array patches under the assay chamber. (iii) Concept of digital counting of cell secreted cytokines. The distance between patches is not drawn to scale. B) dPP assay procedure: (i) settling cells and beads into designated microwell arrays; (ii) isolating assay chambers, stimulating cells with multiplexed stimulation conditions, and incubating cells; (iii) one-step sandwich immunocomplex formation; and (iv) washing, enzyme labeling, cell staining and digital counting of secreted proteins. The digital biosensing of secreted proteins for 48 on-chip assay chambers takes ≈ 2 h after the incubation of stimulated cells.

patches for assay calibration (Figure 1B (ii)). The channel layer replacement procedure can be manually performed within 30 s without using a microscope. The channel layer features are designed to tolerate alignment error (See Experimental Section for alignment tolerance details). When the bulk culture medium is removed from the microfluidic channels before the de-bonding of Channel Layer 1, the trapped cells are retained in the microwells, each filled with a culture medium droplet that is formed due to surface tension (Figure 1B (ii)). The cell encapsulation in the droplets provides the protection for the cells from undesirable mechanical stress that may occur during the debonding step. That is why we observed good cell viability after the channel layer replacement procedure (see Figure S3, Supporting Information). Each assay chamber is designed to contain an asymmetric-sized inlet/outlet. The chamber inlet with a larger diameter (4 mm) makes fluid manipulation easy and provides a reservoir (30 μ L) for the reagent. To activate the seeded target

cells, a culture medium with stimulant reagent solutions at different concentrations are loaded to these on-chip cell culture chambers using a multichannel pipette (Figure 1B (ii)). The whole dPP chip is then scanned to capture images of the cell array patches. The images are analyzed by a computer vision cell-counting code discussed later to precisely count the number of cells in each assay chamber. Subsequently, the dPP chip is placed in a moisture-controlled Petri dish to incubate the cells in an incubator for a given period of time, which fill the assay chambers with cell-secreted analytes.

To detect the analytes released from the stimulated cells, a bead-based one-step sandwich digital immunoassay is performed in the assay chambers in parallel (Figure 1B (iii)), where loading a mixture of hamster sourced capture antibodies and rabbit sourced detection antibodies triggers the capturing of the cell-secreted antigens on the beads by forming bead-antibody-antigen-antibody immunocomplexes. The immunochemistry reaction above is quenched after incubating for 30 min through

fluid removal. Channel Layer 2 is then replaced by Channel Layer 1 for washing, enzyme labeling, microwell isolating, and cell staining (Figure 1B (iv), see Experimental Section for further dPP assay details). Then, the dPP chip is imaged and scanned at the digital sensor array/cell array patches by a standard motorized fluorescence microscope to precisely count both antigen-bound beads emitting an “ON” fluorescence signal (Figure S4, Supporting Information) and the number of stained cells in each on-chip assay chamber. After processing the data, the cytokine quantity measured in each chamber is normalized to the previously counted cell number to quantify the cellular secretions from the corresponding assay chamber. In this study, we used the image scanning process to demonstrate the ability to additionally characterize the phagocytic activity of target cells. The phagocytic phenotype characterization involved the use of pHrodo Red labeled A β fibrils (see Experimental Section for details). The pHrodo Red is a pH-sensitive fluorogenic probe that dramatically increases fluorescence as the pH level drops. pHrodo Red labeled A β fibrils phagocytosed by cells are in acidic phagosomes and will therefore emit red fluorescent signal. The A β phagocytic activity level was assessed from the fraction of red fluorescence-emitting cells observed from the dPP chip images.

2.2. Characterization of dPP Device Performance

We optimized the population of capture antibodies immobilized on the beads to achieve the best dynamic range/sensitivity combination for the on-chip digital sensors incorporated into the dPP platform (Figure S5, Supporting Information). By measuring a cell culture medium spiked with TNF- α at various concentrations, we obtained the sensor linear dynamic range across 3 orders while reaching a sensor limit of detection (LOD) of 0.25 pg mL⁻¹ (Figure 2A). The calibration curve was fitted with 4 parameters logistics ($R^2 = 0.9952$), and the LOD was determined as the signal corresponding to three times the standard deviation of the blank. Furthermore, culture medium samples containing TNF- α secreted by RAW264.7 macrophage cell line were tested using both the dPP platform and the gold standard ELISA to validate our method. In the ELISA measurements (Figure S6, Supporting Information), larger sample volumes >50 μ L of cell-secreted TNF- α were required and were therefore prepared separately in a conventional 96 cell culture well plate (see Experimental Section for cell secreted sample preparation details). The correlation between the two assay methods shows excellent agreement with $R^2 = 0.9524$ across 12 measurements and the slope k of the linear trend line at 0.9242 (Figure 2B).

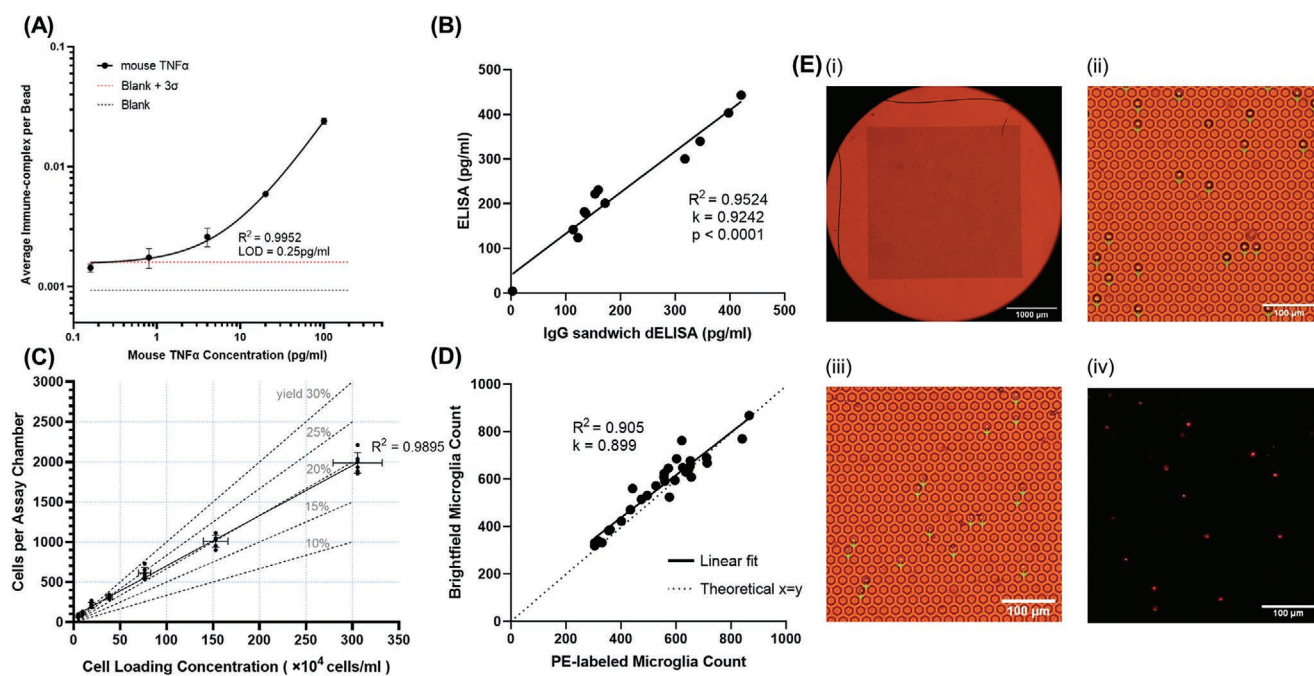


Figure 2. A) Integrated digital immunosensor standard curve for TNF- α in cell culture medium at the concentration ranging from 0.16 to 100 pg mL⁻¹. The data points were fitted with a four-parameter logistic (4PL) curve ($R^2 = 0.9952$). The black dotted and red dotted lines represent the signal level from a blank solution and 3σ above the blank signal level, respectively. The digital immunosensor limit of detection (LOD) of 0.25 pg mL⁻¹ was determined using the red dotted line. B) Measurements of cell-secreted TNF- α using ELISA and the IgG sandwich digital ELISA show good agreement ($R^2 = 0.9524$, slope $k = 0.9242$, $p < 0.0001$). C) Linear relationship ($R^2 = 0.9895$) between the number of trapped cells in each assay chamber and the cell loading concentration. Each channel is flowed with 20 μ L of cell suspension which will later be isolated into 6 individual assay chambers. The yield (trapped cells/total loaded cells) was $\approx 20\%$. D) Good agreement ($R^2 = 0.905$, slope $k = 0.899$) between two schemes for counting the number of microglia: a) brightfield computer vision counting and b) fluorescent labeling and counting with an intensity threshold pre-defined. Primary microglia are smaller in size than RAW 264.7 cells and more subject to debris contaminations in samples. The brightfield computer vision cell counting provided consistent label-free, unbiased determination of the cell number with high accuracy even for the more challenging case of microglia counting. E) Representative images of the cell array patch of an assay chamber with single-cell trapping microwell arrays: (i) whole brightfield image; (ii) zoomed-in brightfield image with RAW264.7 cells; (iii) zoomed-in brightfield image with microglia cells; (iv) zoomed-in fluorescent image with PE-labeled microglia, which served as a reference to validate the accuracy of the label-free brightfield computer vision cell counting algorithm.

Next, we determined the cell trapping yield of the dPP device by measuring the fraction of the number of trapped cells to the total number of loaded cells onto the chip (Figure 2C). Trapped cells were counted for a given concentration of loaded cells (assessed using a hemocytometer) with 6 repeats. The yield was theoretically predicted by taking the fraction of the total trapping area added up over the entire trapping microwells to the total area of the microfluidic cell patterning channel on the Channel Layer 1. The experimentally obtained yield is 19.5% for the dPP device, which is in good agreement with the theoretical value of 20% as designed. The total number of trapped cells was found to be proportional to the concentration of loaded cells. It matches the theoretical prediction with $R^2 = 0.9895$.

A computer vision code was used for 5X brightfield images to recognize and count the exact cell number in all assay chambers on the dPP chip in parallel (Figure S7, Supporting Information). Figure 2E (i) is a representative high-resolution image of a cell array patch taken by a consumer grade CMOS camera (SONY $\alpha 7$ III) using 5X objective lens in our dPP chip scanning setup. Figure 2E (ii) and (iii) show representative close-up brightfield images recognized by the computer vision code with RAW 264.7 cells and primary microglia trapped in microwell arrays, respectively. We validated the accuracy of our brightfield counting code using PE(phycoerythrin) anti-mouse CD64 antibody labeled primary microglia as target cells. Microglia are glial cells providing the active immune defense in the central nervous system. They are smaller in size ($\approx 5 \mu\text{m}$ in diameter) as compared to RAW 264.7 cell lines ($\approx 10 \mu\text{m}$ in diameter) and are likely misrecognized as debris in microfluidic channels. Therefore, the image recognition for counting microglia is more challenging. Nonetheless, good agreement was obtained between PE fluorescent image cell counting (Figure 2E (iv)) and code assisted-brightfield image cell counting (Figure 2E (iii)) with $R^2 = 0.905$ and slope $k = 0.899$ (Figure 2D). This confirms the ability of the computer vision brightfield analysis to consistently and accurately quantify the cell number across on-chip assay chambers without subjective human error.

2.3. RAW 264.7 Secretory Phenotyping and Phagocytosis Assay

We tested the functional phenotypes of RAW 264.7 mouse macrophage cell lines in response to varying stimulation conditions with 0.8–100 ng mL⁻¹ of LPS, 0.25–1 μM of A β (see Experimental Section for A β preparation details), 0.8–100 ng mL⁻¹ LPS plus 0.5 μM A β , and negative control (for determining the basal secretion level). Cells remain highly viable in dPP and the mean cell viability across all conditions after 26 h was 94.7% assessed by Calcein AM staining and fluorescent imaging (Figure 3A (ii)). We did not observe a significant difference in cell viability between different stimulation conditions. This eliminates our assay from the influence of cell viability changes resulting from the varying stimulation conditions on the following analysis of TNF- α secretion and A β phagocytic activity. We also verified that the presence of these stimulants would not significantly influence the signal strength or sensitivity of our digital immunosensor (Figure S8, Supporting Information).

By testing the varying population of LPS-stimulated RAW264.7 macrophage cell lines, we can estimate the lower

bound for the cell population to avoid large data variance amplified at low cell numbers due to single-cell phenotypical heterogeneity. We measured the concentrations of TNF- α secreted from 100 ng mL⁻¹ LPS stimulated RAW 264.7 cells in assay chambers with their number varied from 17 to 610 and observed that the TNF- α concentration approximately linearly increased with the number of cells > 200 in an assay chamber (Figure 3B). The linear relationship indicates no significant paracrine signaling or feedback between nearby cells in this range of cell density.^[45] The relatively scattered concentration behavior observed for < 100 cells in the chamber (Figure 3B, inset) may reflect the single-cell-level phenotypical heterogeneity pronounced with the smaller number of tested cells.^[45] As long as our measurement is undertaken in the linear range, normalizing the quantities of secreted TNF- α per cell provides statistically consistent phenotypic metric of the cells. As such, testing ≈ 200 RAW cells and ≈ 500 microglia in each assay chamber allowed us to confidently monitor the basal TNF- α secretion levels from those cells with the sensitivity of our digital sensors. The median TNF- α concentration across our measurements under all selected stimulation conditions is $\approx 20 \text{ pg mL}^{-1}$ for both RAW 264.7 cell and primary microglia tests, which is sufficiently above the LOD of the sensors (Figure 3C). As expected, the TNF- α secretion activity of RAW 264.7 cells elevates with the increased dosage of LPS or A β alone (Figure 3D). The RAW 264.7 cells appear more activated by LPS than A β . The combination of LPS and A β activates the cells more vigorously. We also observed a low basal secretion which is significantly lower than all other stimulation conditions, indicating the chemical stimulations is more prominent to the dPP assay procedure stimulation if any.

In parallel to the TNF- α secretion digital assay above, we performed phagocytosis assay with the same devices (Figure 3E). The A β phagocytic activity was quantified by the fraction of the number of cells showing A β intake with the red pHrodo fluorescent signal to the total number of cells counted by brightfield imaging. The weak signal intensity could yield counting error with a conventional image processing algorithm, we therefore used a modified version of our machine learning code developed in our previous work.^[41–43] We observed almost no fluorescent background ($\approx 0.1\%$) in all of A β -free samples whether or not LPS presented in them. The fraction of phagocytosis-active cells steadily increased from 11.9% to 55.0% with A β increasing from 0.25 μM to 1 μM . Interestingly, we discovered that LPS activated TNF- α secretion had little effect on the A β phagocytic activity of RAW 264.7 cells. The average A β phagocytic activity of the LPS/A β co-stimulated cohort was 31.6%, which is almost identical with that of the 0.5 μM A β stimulated cohort (31.3%). Furthermore, no statistically significant difference was found in the A β phagocytic activity of co-stimulated cells exposed to LPS at varying concentrations.

2.4. 5xFAD and Wild Type Mice Secretory Phenotyping and Phagocytosis Assay

Microglia are resident phagocytes of the central nervous system that serve as important mediators of inflammation in multiple conditions. Their functions in cytokine secretion and

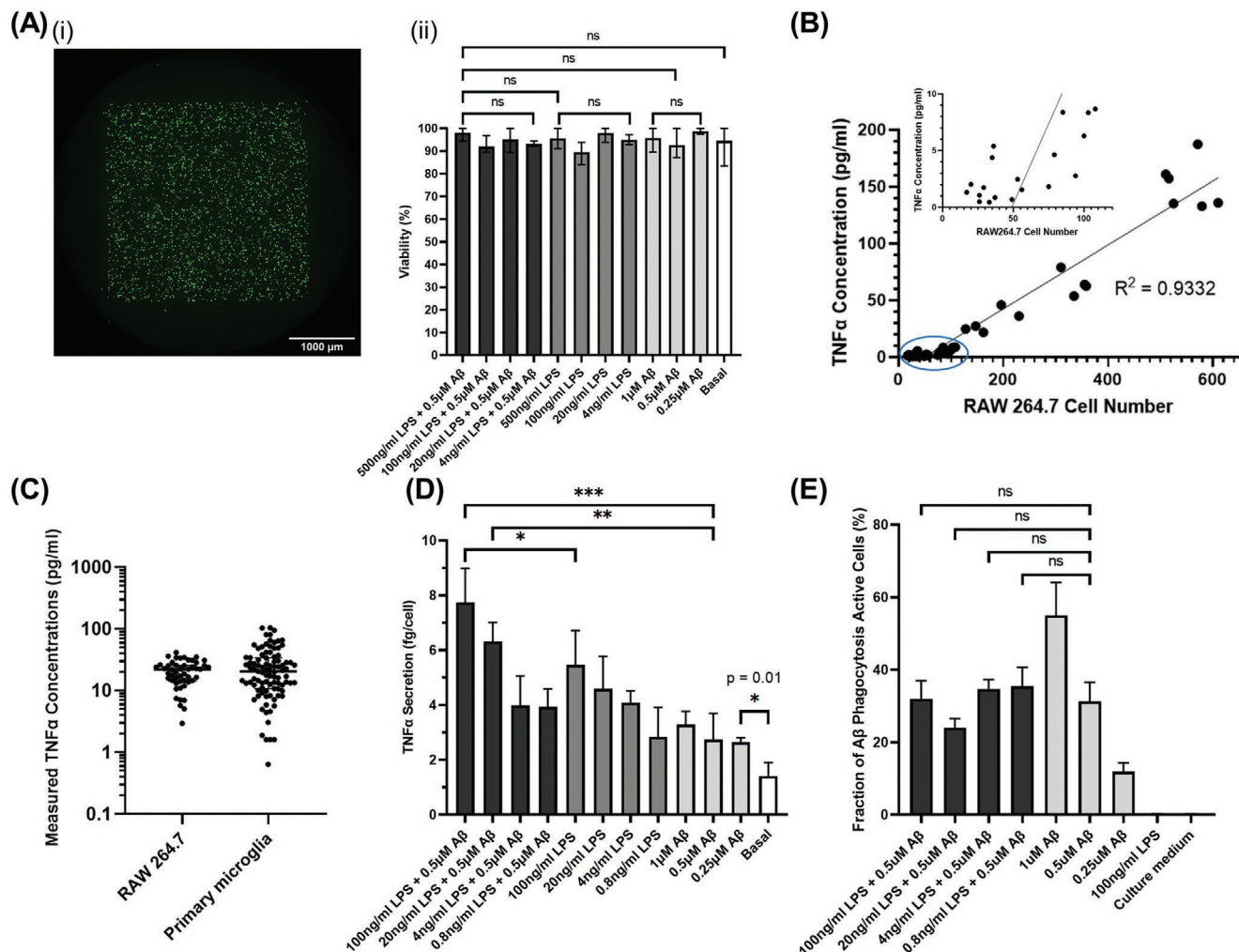


Figure 3. A) (i) Representative high resolution fluorescent image of Calcein AM stained live RAW 264.7 cells in dPP cell arrays. (ii) No significant difference in the cell viability was observed across all stimulation conditions. The cell viability was determined from the fraction of the number of green fluorescence-emitting live cells at the endpoint of the digital immunoassay to the total number of tested cells counted with the brightfield image. The error bars represent the standard deviation of the data. B) TNF- α concentrations measured for the varying number of RAW 264.7 cells stimulated by 100 ng mL $^{-1}$ of LPS in an assay chamber. The digital immunosensors could measure TNF- α secreted from cells with a number as small as 17 in the 30 μL assay chamber. The measured TNF- α concentration linearly increases with the cell number > 100 ($R^2 = 0.9332$), indicating no significant paracrine effect on the measurements. The inset plot shows a larger variability of the cell-secreted TNF- α concentration profile as a result of the single cell-level heterogeneity that is pronounced for groups of the small (17–100) number of cells. C) Distribution of TNF- α concentrations measured across all stimulation conditions used in the RAW264.7 cell line and microglia tests. Approximately 50% of the concentrations measured were below 20 pg mL $^{-1}$. D) TNF- α secretion level per cell measured for RAW 264.7 cells under different stimulation conditions. E) Results of A β phagocytosis analysis for RAW 264.7 cells under different stimulation conditions. The A β phagocytic activity was assessed by number of cells that has A β intake (emits red fluorescent signal due to pHrodo labeling on A β) divided by total number of cells. The data show no significant difference in the A β phagocytic activity of RAW 264.7 cells between LPS/A β costimulation and A β stimulation conditions. A high signal-to-noise ratio was achieved in the assay (<0.1% of background signal in negative controls). All error bars represent the standard deviation unless otherwise specified.

phagocytosis of A β are believed to affect the outcome of Alzheimer's disease (AD).^[46,47] Cytokines released by microglia during their inflammatory reaction, including TNF- α , lead to neurotoxicity and synapse loss.^[10,48–51] Using the dPP platform, we performed assays characterizing the TNF- α secretory phenotype and A β phagocytic activity of primary microglia isolated from the brains of 11 aged (\approx 1 year old) mice, including 6 with 5xFAD genotype and 5 with wild type genotype (Figure 4A) (see Experimental Section for microglia isolation and enrichment method from brain tissues). Based on the results for the RAW 264.7 cells above, we selected 4 stimulation conditions

here (100 ng mL $^{-1}$ LPS + 0.5 μM A β ; 0.5 μM A β ; 100 ng mL $^{-1}$ LPS; and basal). We trapped \approx 500 isolated microglial cells in each assay chamber and performed the assay under one of the stimulation conditions for each animal. For animals yielding more cells after an enrichment process, we performed extra repeats of the assay. Although microglia are known to function as macrophages in the central nervous system, the cells tested here produced, on average, about the half amount of TNF- α produced by the RAW264.7 cells under the same stimulation conditions. In contrary to the case of RAW 264.7 cells, we observed the microglia's secretory behavior was more activated

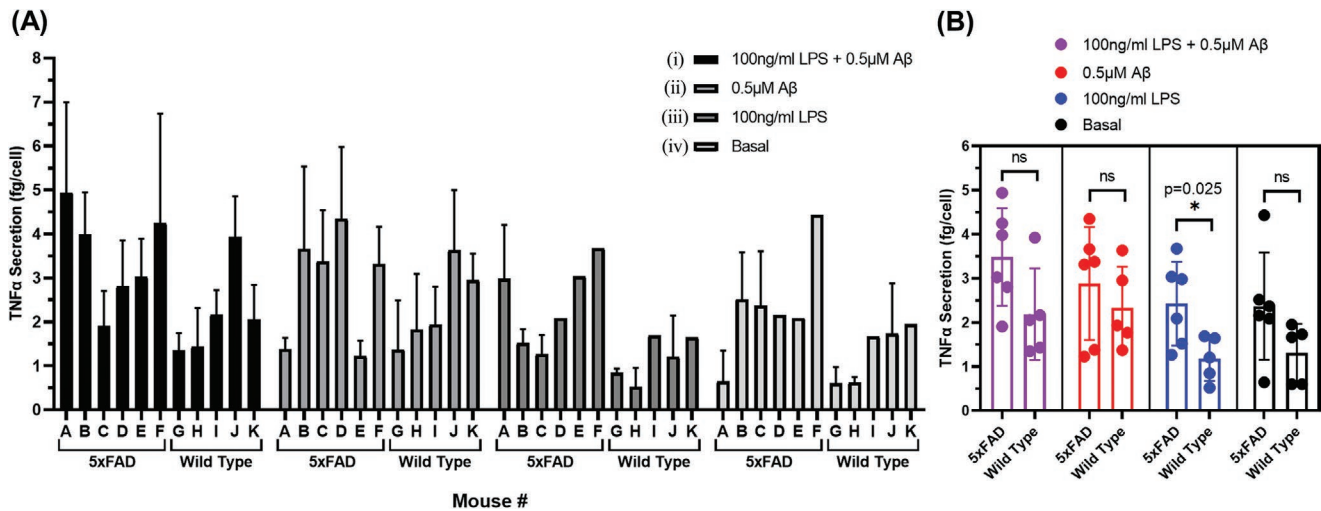


Figure 4. A) TNF- α secretory phenotyping on primary microglia isolated from 11 adult mice (6 5xFAD and 5 wild type mice \approx 1 year old). The stimulation conditions to elicit the cell phenotypes include (i) 100 ng mL⁻¹ LPS + 0.5 μ M A β , (ii) 0.5 μ M A β , (iii) 100 ng mL⁻¹ LPS, and (iv) basal. B) Group comparison of TNF- α secretion between 5xFAD genotype (Alzheimer's Disease model) mice and wild type mice under the 4 stimulation conditions. The data show the TNF- α secretion level averaged over the 5xFAD mice across all 4 conditions is higher than that of the wild type mice. A statistical analysis using the *t*-test indicates that the stimulation condition only with LPS treatment yields a significant difference between 5xFAD genotype and wild type cohorts. The analysis did not take into account animal-to-animal variability. Therefore, a linear mixed model was further used to analyze the data (Table 1). All error bars represent the standard deviation.

by A β than by LPS. The larger variability of the microglia data than the RAW264.7 cell data could be attributed to activation of the cells during the rigorous isolation process or heterogeneity across the tested animals, as opposed to testing clonal cells growing in steady-state culture.

We compared the TNF- α secretory phenotype between the 5xFAD genotype and wild type cohorts under each stimulation condition (Figure 4B). Although the average values were higher for 5xFAD mice across all 4 conditions, only the stimulation with 100ng mL⁻¹ of LPS yielded a statistically significant difference between the two cohorts ($p = 0.025$). This analysis does not account for animal-to-animal heterogeneity and is also potentially confounded by biases due to repeated measures from the same animals or false discovery due to multiple pairwise comparisons. To take advantage of the entire dataset obtained by the dPP platform, which contains multiple exposures and technical replicates within each animal, we analyzed the results by using a linear mixed model with random effects for each animal and fixed effects of genotype and LPS and A β exposure (Table 1 see Experimental Section for details). This analysis revealed main effects of genotype and A β exposure on TNF- α secretion, and no effect of LPS or interaction among stimulation conditions or genotype. Notably, we did not observe a main effect of LPS (100 ng mL⁻¹) stimulation in microglia. Though LPS at higher doses has been shown to produce a measurable secreted TNF- α response in acutely isolated microglia from adult mice,^[52] we intentionally picked a moderate dose so as not to drown out a possible interaction with A β . The lack of detected response is thus likely due to under-stimulation of acutely isolated adult microglia.

The A β phagocytosis assay was also conducted in parallel for the primary microglial cells on the dPP chip. Some of the cells show in the analysis of TNF- α secretions were isolated using an enrichment protocol involving PE-based releasable beads

that interfered with the pHrodo fluorescent probe used in the phagocytosis assay. Eliminating these cells from the assay test, we obtained data for 3 of the 6 5xFAD and 2 of the 5 wild type mice (Figure 5B). Some fluorescent background was still observed for samples exposed to A β -free stimulants. It possibly originated from auto fluorescent debris in the brain tissue, which occupied \approx 2.43% of the population of the counted microglia on the device. However, the debris background was low as compared to the A β phagocytic activity signal (10% of the microglia population). Intriguingly, a distinctive difference in A β phagocytic activity was shown between 5xFAD and wild type mice under both 100ng mL⁻¹ LPS + 0.5 μ M A β and 0.5 μ M A β stimulation conditions (Figure 5C). The result indicates that the

Table 1. Linear mixed model analysis of TNF- α secretion level from primary microglia. When all technical and biological replicates are taken into account in all stimulation conditions, 5xFAD genotype and A β stimulation were found to result in significant increases in TNF- α , while LPS stimulation did not. There were no significant interaction effects among the stimuli or 5xFAD genotype.

Parameter	<i>p</i>	95% confidence interval for effect size estimate [fg cell ⁻¹]	
		Lower bound	Upper bound
Intercept	0	2.94	4.32
Genotype	0.011	0.31	2.32
LPS	0.186	-0.32	1.65
Amyloid	0.01	0.33	2.39
Genotype x LPS	0.278	-0.64	2.22
Genotype x Amyloid	0.922	-1.42	1.57
LPS x Amyloid	0.374	-0.80	2.12
Genotype x LPS x Amyloid	0.524	-1.44	2.81

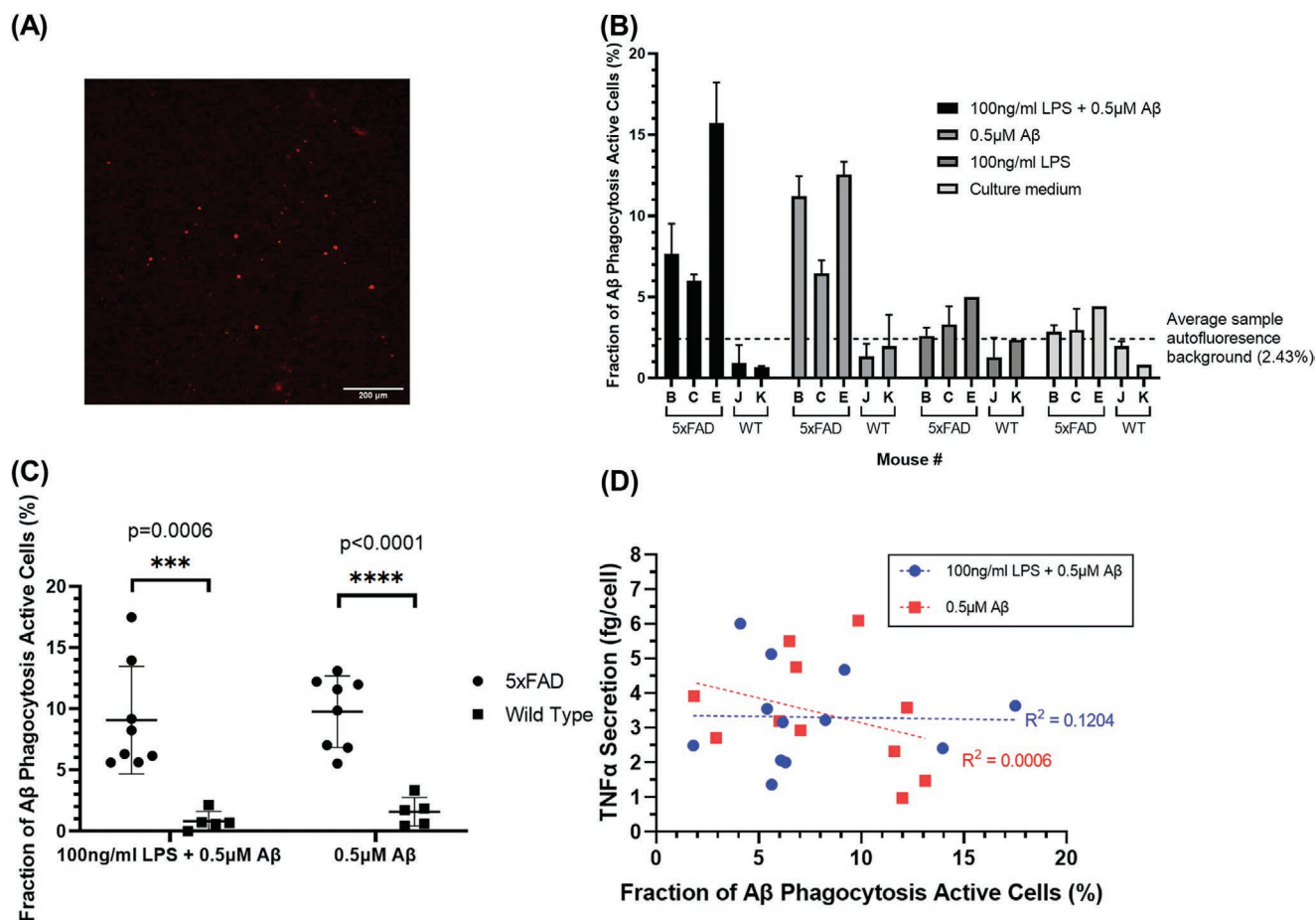


Figure 5. A) Representative fluorescent image of microglia with pHrodo-labeled A β fibril intake, the image was contrast enhanced for clear visualization. B) A β phagocytic activity on 3 5xFAD mice and 2 wild type (WT) mice. A higher background in negative control microglia samples (without A β stimulation) was observed. The average background level is 2.43% of the total trapped cells, possibly caused by auto fluorescent brain debris in processed microglia samples. C) Group analysis of A β phagocytic activity between 5xFAD mice and wild type mice microglia stimulated with 100 ng mL⁻¹ LPS + 0.5 μ M A β or 0.5 μ M A β alone. A statistically significant increase was observed for the A β phagocytic activity of 5xFAD microglia as compared to that of wild type microglia in both LPS + A β costimulation ($p = 0.0006$) and A β stimulation ($p < 0.0001$) conditions. D) Correlation between A β phagocytic activity and TNF- α secretion characterized in each dPP assay chamber for the same microglia. The poor correlation for both stimulation conditions (LPS + A β : $R^2 = 0.1204$, A β : $R^2 = 0.0006$) indicates that there is no universally “activated” status of microglia. All error bars represent the standard deviation.

microglia from the aged 5xFAD mice still maintained the ability to phagocytose fibrillar A β in vitro after prolonged exposure to A β in vivo. Together with the results from the TNF- α secretion assay above, we analyzed the correlation between the secretory and phagocytic phenotypes for both LPS+A β co-stimulated and A β stimulated cells (Figure 5D). The correlation is poor (LPS + A β : $R^2 = 0.1204$, A β : $R^2 = 0.0006$), suggesting that the activation of a certain cellular function cannot be guaranteed by the activation of the other. Therefore, multiparameter phenotyping is necessary to fully understand the multifaceted nature of the cellular functions in the brain, especially for AD disease models.

3. Conclusion

Assessment of the cytokine secretion function of cells is crucial in studying numerous inflammation-mediated diseases. However, the assay becomes challenging when the detection

of cell-secreted proteins requires high assay sensitivity, accuracy, throughput, and flexibility. To fill this technological gap, our study has developed an integrated microfluidic platform, namely, the “digital Phenoplate (dPP).” The dPP is the first cellular secretory phenotyping platform that integrates digital molecular counting immunosensors, cell trapping, culture and cytometry on a single microfluidic chip. Each dPP chip contains 48 arrays of microfluidic cell assay chambers, which enables on-chip parallel multiparameter analysis operations, including precision counting of cells, sensitive digital immunosensor-based quantification of cytokine molecules in a culture medium, and image-based cytometry with machine learning and computer vision codes, all together. To precisely control the antigen-antibody reaction timing in those chambers, we employed a novel one-step sandwich digital immunoassay protocol for on-chip TNF- α detection. This integration method ensures no molecular interference between the sensors and the cells during the secretion period and offers flexibility in controlling the cell

secretion duration and the antibody immunochemistry reaction time. A correlation between the reaction time and sensitivity of the digital immunosensors has been extensively characterized in our previous work.^[41] Our digital immunosensor-based TNF- α assay achieves a LOD as small as 0.25 pg mL⁻¹, and its data correlate well with results of the gold standard ELISA. The high sensitivity and large dynamic range of the digital immunosensors permitted the assay with the number of RAW 264.7 cells ranging from 17 to 610 in each assay chamber. Our on-chip cell trapping followed a mechanical benign procedure leaving a majority (94.7%) of the cells healthy for at least 26 h.

To demonstrate the utility of the dPP platform, we simultaneously characterized the phenotypes of microglial cells isolated from the brains of Alzheimer's disease model (5xFAD) and wild type mice by measuring both TNF- α secretion and A β phagocytosis under multiple stimulant conditions. The question of whether Alzheimer's disease and exposure to A β leads to microglial activation or senescence is central to conflicting theories of the progression of neurodegenerative disease.^[53–55] The physiologic role of microglia in brain homeostasis and neuroinflammation in health and disease states encompasses multiple functions, including secretion of cytokines, immune surveillance of the brain microenvironment, phagocytosis of pathogens and extracellular protein, and regulation of synaptic function.^[56] However, even assessing the simplest microglial phenotypes related to cytokine secretion and phagocytosis is complicated by synergistic interactions among A β and cytokine stimuli,^[57,58] A β aggregation state,^[59] and age and strain of donor animals.^[60,61] Therefore, combinatorial experimental designs are frequently necessary to understand the interaction of multiple factors, the complexity of which can potentially introduce false-positive and false-negative results due to the heterogeneity of responses in individual animals and the difficulty of testing cells from individual animals in multiple conditions.

The dPP platform can address these difficulties in several ways to improve rigor and reproducibility. First, by allowing sensitive assays using a very small number of cells, it is possible to perform replicated measurements using cells from a single animal across multiple experimental conditions simultaneously. Second, by incorporating simultaneous measurements of both secreted protein and image-based cytometry, the dPP allows within-sample comparison of multiple outcomes. For example, we found a poor correlation between TNF- α secretion level and A β phagocytic activity, highlighting the lack of a bimodal “activated” state in primary microglia, as posited in recent studies.^[62] While we have used image-based cytometry here to characterize cellular phagocytosis, this image-based cytometry could be extended to other assays, for example, by using fluorescence-based probes for membrane potential or respiratory chain function to determine the biophysical properties of cells in the dPP.^[63] Third, the ability to incorporate combinatorial designs into experiments utilizing primary cells enables analysis with mixed-effects linear models that address animal-to-animal/sample-to-sample heterogeneity, as well as the problem of false-positive associations due to multiple comparisons. This approach to analysis, enabled by recording multiple technical replicates in every stimulation condition from every animal, maximizes data utilization of our parallel measurements and

revealed a significant increase in TNF- α secretion when the microglia have a 5xFAD genotype or are acutely exposed to A β . Repeated within-animal measures require sensitive, low input, but high throughput measurements to uncover significant relationship in noisy biological systems.

The dPP does have several limitations. Due to the wide variety of cell preparation and separation methods that are required for both circulating and tissue-resident immune cells, we have intentionally required that all cell separation steps be performed before loading the dPP. Given that we measure combined secreted protein from the captured cells, the relative heterogeneity of the cell population that underlies this result will depend on the cell separation method used. Deep phenotyping of cellular heterogeneity in most cell populations would require high throughput single cell transcriptomic profiling, such as by single cell RNAseq. While high throughput intracellular protein measurement via flow cytometry is possible, it does require the use of protein secretion inhibitors which may change cell responses. However, the ability of the dPP to study secretion from small numbers of cells does allow the study of heterogeneity by separating small populations of cells by fluorescence activated cell sorting. We have also intentionally designed the dPP to capture cells from a cell suspension. The same approach that underlies the dPP, however, could be used to assay secretions from cellular aggregates, such as isolated microvessels^[64] or pancreatic islets^[65] with modifications to the geometry of the cell assay chambers to accommodate aggregates rather than single cells.

The integrated dPP exhibits promising potential in interrogating and distinguishing subtle cell phenotypes with precision. While we have focused here on isolating and phenotyping primary microglia in a model of neurodegeneration, the dPP is suitable for multiparametric immunophenotyping of low-abundance cells isolated from a variety of clinical samples or preclinical models. With further modifications in cell capturing structures to increase capturing yield and inclusion of other analyte panels, the dPP platform will open new opportunities in studying collective secretory phenotypes that comprises rare or low cytokine secreting cells, low abundance analytes of interest or monitoring rapid response post stimulation across a variety of disease states.

4. Experimental Section

Materials: TNF alpha Mouse Uncoated ELISA Kit with Plates (Catalog # 88-7324-22) and the Rabbit anti-Hamster IgG (H+L) Secondary Antibody were purchased from Invitrogen. We obtained anti-CD11b (clone M1/70, BV605), anti-CD45 (clone 30-F11, BV421 conjugated), anti-CD64 (clone X54-5/7.1, biotin or PE conjugated), and anti CD16/CD32 (clone 93) antibodies from Biolegend. Dynabeads, 2.8 μ m diameter epoxy-linked superparamagnetic beads, avidin–horseradish peroxidase (HRP), QuantaRed™ enhanced chemifluorescent HRP substrate, pHrodo Red (succinimidyl ester), bovine serum albumin (BSA), and PBS SuperBlock blocking buffer were purchased from Thermo Fisher Scientific. We obtained Sylgard 184 clear PDMS from Dow Corning, 4 \times 3" large glass slides (102 \times 76 mm) from Ted Pella, and Fluorocarbon oil (Novoc 7500) from 3M. We purchased high glucose DMEM and RAW 264.7 cell line from ATCC, Fetal Bovine Serum (FBS) and Penicillin-Streptomycin (Pen-Strep) from Gibco, Lipopolysaccharides (LPS, *E. coli* O111:B4) from Sigma-Aldrich, human A β aggregation kit (Catalog

#A-1170-025) from rPeptide. 5xFAD mice (MMRRC Stock no. 034848-JAX) are on the C57BL/6 background and were originally obtained from Jackson Labs and have been maintained by breeding to littermates to keep the same background. WT mice are littermates of the 5xFAD. Both sexes were used. Neural Tissue Dissociation Kits (Catalog #130-092-628) were purchased from Miltenyi. Rat serum, EasySep Release Mouse Biotin Positive Selection Kits (Catalog #17 655) and EasySep Release Mouse PE Positive Selection Kit (Catalog #17 656) were purchased from STEMCELL.

Antibody Conjugation to Magnetic Beads: We conjugated the anti-Hamster IgG Secondary Antibody antibodies using the epoxy-linked Dynabeads (2.8 μm) with the capture antibody molecules at a mass ratio of 6 μg (antibody): 1 mg (bead) following the protocols provided by Invitrogen (Catalog #14311D). The beads were then quenched (for unreacted epoxy groups) and blocked with TBS StartingBlock T20 blocking buffer. We stored the antibody-conjugated magnetic beads at 10 mg beads per mL in PBS (0.05% T20 + 0.1% BSA + 0.01% sodium azide) buffer at 4 °C. No significant degradation of the beads was observed within the 3 month usage.

Preparation and pHrodo Labeling of Amyloid Beta Fibrils: The human A β aggregation kit (Catalog #A-1170-025, rPeptide) was equilibrated to room temperature and NaOH (250 μL , 10 mM) was added and swirled in the tube to ensure hydration of the lyophilized material. HPLC water (250 μL) and 10X TBS pH 7.4 (56 μL) were added to the rehydrated A β to neutralize the solution. After mixing well with a pipette, the sample yielded a 100 μM A β solution. The prepared A β solution was incubated at 37 °C overnight to allow for aggregation. After aggregation, 0.1 M sodium bicarbonate was prepared and filtered through a 0.2 μm filter unit. The aggregated A β solution was centrifuged at 16 000 \times g for 1 min to collect the aggregates. The supernatant was discarded and HBSS was added to rinse the aggregates twice. The aggregates were then resuspended in sodium bicarbonate (200 μL , 0.1 M). 10 mg mL⁻¹ of pHrodo Red dye was prepared by diluting pHrodo Red in DMSO and the pHrodo Red dye (36 μL) was added to the A β aggregate suspension to initiate the labeling reaction. The final ratio is \approx 10 dye molecules per A β molecule. The reaction was incubated for at least 1 h at room temperature in the dark. After reaction, the aggregates were centrifuged at 16 000 \times g for 1 min and washed with methanol to remove excess dye. The aggregates were again centrifuged at 16 000 \times g for 1 min and washed with 1 mL HBSS for 4 times. After the final wash, the supernatant was removed and HBSS (200 μL) was added to mix. The A β was put in a sonicator bath at room temperature for 5–10 min to improve the consistency of the A β suspension. The pHrodo Red-labeled A β was stored in single use aliquots at -80 °C for up to 6 months.

dPP Chip Fabrication and Patterning: The PDMS thin film (\approx 300 μm) with bead microwell arrays (3.4 μm diameter, 3.8 μm in depth and 8 μm in pitch) and cell microwell arrays (hexagons with 16 μm diameters, 20 μm in depth, and 22 μm in pitch) was made through standard SU-8 molding. We constructed the SU-8 molds on oxygen plasma treated silicon wafers first by standard photolithography depositing negative photoresist (SU-8 2005 MicroChem) layers at 5000 rpm to form the bead microarrays with thicknesses 3.8 ± 0.1 μm . The thicker cell microarrays were then formed through depositing new negative photoresist (SU-8 2010 MicroChem) on the wafer at 1000 rpm (thickness 20 ± 0.5 μm) followed by mask alignment and a second standard photolithography process. Subsequently, a precursor of PDMS was prepared at a 10: 1 base-to-curing-agent ratio and deposited onto the SU-8 mold by spin coating (200 rpm) and overnight baking at 60 °C. The fully cured PDMS thin film was then transferred onto the large glass slides (Ted Pella 4 \times 3", 102 \times 76 mm) using air plasma bonding. The PDMS Channel Layer 1 and Channel Layer 2 (both has channel height 83 ± 1 μm) were also made through standard SU-8 molding similar to the procedure stated above using negative resist (SU-8 2050 MicroChem) deposited on the wafer molds at 1700 rpm followed by a standard photolithography process. The dPP bead patterning process (Figure 1B (i)) involved manually applying pressure to seal the PDMS Channel Layer 1 (for bead and cell patterning) against the PDMS microwell array layer on the bottom glass substrate. Then, we prepared 10 sets of a 25 μL

bead solution at the concentration of 2 mg mL⁻¹ bead respectively. The bead solution was loaded into ten different physically separated bead patterning channels (8 sample channels and 2 calibration channels). After the beads settle inside the microwells, we washed the patterning channels with 100 μL PBS-T (0.1% Tween20) to remove the untrapped beads. We then block each channel with Superblock buffer and incubate overnight to avoid nonspecific protein adsorption during the following secretion assays. The DPP chip was typically prepared in batch and can be sealed in a moisture-controlled Petri dish at room temperature (RT) for up to a week with no significant degradation.

Mouse Brain Tissue Process: Brain tissues were obtained from male and female 12–15-month-old 5xFAD mice on a C57BL/6 background (B6.Cg-Tg(APP^SSwFLon,PSEN1^{*}M146L^{*}L286V)6799Vas/Mmjax, Jackson Labs) or wild-type littermate controls. All procedures involving animals were undertaken in strict accordance with the recommendations of the Guide for the Care and Use of Laboratory Animals by the National Institutes of Health. The study protocol was approved by the University Committee on the Use and Care of Animals of the University of Michigan (protocol #PRO00008999). The CO₂ euthanized mice were perfused transcardially until liver clears with cold HBSS (20–30 mL per mouse). The brain tissues were dissected, rolled on a filter paper to remove meninges and each was minced immediately into cold HBSS (10 mL). Enzyme Mix 1 and Enzyme Mix 2 were prepared according to the protocol from the vendor (Neural Tissue Dissociation Kits, Catalog #130-092-628, Miltenyi). The tissue fragments were pelleted at 300 \times g, and then preheated Enzyme Mix 1 (2 mL per brain) was added to them. The samples were subsequently incubated for 15 min at 37 °C under slow continuous rotation. With enzyme Mix 2 (30 μL per sample) added, the tissues were gently and progressively triturated between a few rounds of incubation through mechanical dissociation using pipettes of different size. The samples were filtered through a 70 μm mesh cell strainer and pelleted at 250 \times g at RT.

Microglia Enrichment Process: Each brain tissue sample prepared above was then resuspended in 37% Percoll (7 mL) with 70% Percoll (3 mL) underlayered. The samples were then centrifuged without brake at 1500 \times g, 18 °C for 30 min. After the myelin on top of the Percoll gradient in each sample was removed, the enriched microglia layer (1–2 mL) was collected and washed with HBSS (12 mL) at 500 \times g for 5 min. The pellets were resuspended and washed again with PBS containing FBS (2%) and EDTA (1 mM) under 500 \times g for 5 min and were resuspended in a 0.25 mL volume. The immunomagnetic positive selection technique was used for microglia enrichment from the suspended pellets after the Percoll gradient process. Two types of commercial kits (STEMCELL Catalog #17 655 or #17 655) were used: 1) a PE-based releasable bead enrichment kit and 2) a Biotin-based releasable bead enrichment kit. The PE-based releasable bead enrichment kit yielded more cells (due to higher efficiency in PE bead release reagent chemistry). But it induced a large red fluorescent background on all enriched cells and was therefore avoided in the phagocytosis assays involving the weaker pHrodo fluorescent probe. A sufficient cell population was obtained with a kit using anti-CD64 antibodies for TNF- α secretion assay. The CD64 positive selection protocol involves labelling CD64 expressing microglia with PE-anti-CD64 antibodies or biotinylated anti-CD64 antibodies, binding the labeled microglia to magnetic beads, isolating the microglia-bead conjugates, and releasing the magnetic from the beads (Figure S1, Supporting Information). The processed high purity microglia were later concentrated to a desired concentration and patterned into the dPP for phenotyping.

RAW 264.7 Cell Culture and Cell Secreted Sample Preparation for ELISA/dPP Correlation: RAW 264.7 cells were cultured in high glucose DMEM (ATCC 30–2002) with 10%FBS (Gibco, catalog no. 10 437 028) as recommended by ATCC. 1% of Penicillin-Streptomycin (Gibco, catalog no. 15 140 122) was added in the culture medium to prevent bacteria contamination. Medium renewal was conducted every 2–3 days and upon confluency in T-75 flasks, cells were gently scraped and aliquoted into new flasks with a subcultivation ratio of 1:6 as recommended by ATCC. Prior to each dPP assay, the cells were gently dislodged with a cell scraper, concentrated to a desired concentration and loaded into the

dPP for phenotyping. RAW 264.7 cell secreted samples for ELISA/dPP correlation were separately prepared due to the large sample volume required for ELISA. RAW 264.7 cells were seeded in a conventional 96 cell culturing well plate at a concentration of 5×10^4 cells mL⁻¹ and was stimulated with various conditions as described in the dPP RAW264.7 cell characterization experiments (Section 2.3). The cell supernatants were collected after 24 h of stimulation in a moisture controlled 37 °C, 5% CO₂ incubator and the TNF- α concentrations were measured with dPP and ELISA (Invitrogen, Catalog # 88-7324-22)

dPP Assay and Imaging: After the cells of interests were loaded and patterned in the dPP, the liquids in the bead patterning channels and cell patterning channels were drawn out with pipettes. The PDMS Channel Layer 1 was then removed and replaced by PDMS Channel Layer 2. The whole chip was resealed with Channel Layer 2 via PDMS self-adherence force. The resealing process paired each cell array with a bead array and isolated them into 48 assay chambers. This alignment and resealing process can be manually performed within 30 s without a microscope and is tolerant to alignment error. As long as the whole sensor array patch (diameter ≈ 2 mm) is covered by the 4 mm diameter open-ended inlet, the assay chamber would properly fulfill its purpose. If any misalignment caused some part of the cell array patch to be outside the assay chamber, our cell counting code would eliminate the uncovered/unstimulated cells from the analysis. During the channel layer replacement process, the cell culture medium surrounding the trapped cells was retained inside the microwells due to surface tension. This enabled the cells to maintain good viability (Figure S3, Supporting Information).

Stimulants or culture medium were then added to the large inlets simultaneously with a multichannel pipette and the liquid would be pressure driven across each assay chamber to recombine with the trapped cells and beads. The dPP was then imaged for brightfield counting of the cells in each assay chamber and then be placed in a moisture-controlled Petri dish and incubated in a 37 °C, 5% CO₂ cell incubator during the cell culture/stimulation period (24 h in this work). After incubation and cell secretion of the cytokines, a cocktail of capture antibodies and biotinylated detection antibodies with optimized concentrations (The final dilution factors for capture antibody and detection antibody are 1/7200 and 1/150 from stock solution, respectively) was simultaneously added to the large inlets of each assay chamber with a multichannel pipette to initiate the sandwich immunoassay reaction (30 min). After the bead-anti IgG-capture antibody-antigen-biotinylated detection antibody immunocomplex was formed, liquid in every assay chamber was removed and the PDMS Channel Layer 2 was replaced with PDMS Channel Layer 1 with a similar process as stated above for downstream high throughput washing, HRP enzyme labeling, oil sealing and cell staining. The digital sensor channels were first washed in parallel with washing buffer (PBS-T 0.1% Tween20) for 5 min with a syringe pump at a flow rate of 50 μ L min⁻¹ to removed unbound antibodies and proteins. Avidin-HRP solution (40 μ L, 100×10^{-12} M) was slowly loaded into the chip with a multichannel pipette for enzyme labeling (2.5 min). The chip was washed again with washing buffer for 5 min under 50 μ L min⁻¹ of flow rate using a syringe pump.

The washing buffer was then washed and replaced with PBS solution to reduce the interference between Tween20 and the chemifluorescent HRP substrate used later. Finally, 40 μ L of the QuantaRed (Qred) substrate solution was loaded to the bead channels followed by sealing and isolating the bead microwells with HFE-7500 fluorinated oil (45 μ L) for the digital counting process on a motorized microscope scanning system reported in our previous works.^[41–43] The system scans the image of the bead-filled microwell arrays on the chip right after the oil sealing step to detect the enzyme–substrate reaction activity. The motorized stage was pre-programmed to follow the designated path to scan the entire dPP (48 cell microarrays or 48 bead arrays). The Qred fluorescent channel (545 nm/605 nm, excitation/emission) was first scanned to count the “on” spots at the array followed by the brightfield to count the beads with a transmission light source. The entire scanning process typically takes ≈ 10 min. Cell staining was

then performed at the cell channels and scanned similarly for viability characterizations.

Data Analysis by the Convolutional Neural Network: We analyzed our collected digital immunoassay images by our previously reported convolution neural network (CNN) algorithm. The algorithm parallelly ran two signal recognition pathways, one pretrained to recognize enzyme active “On” microwells (Qred channel) and the other to recognize defects and contaminations using >5000 labeled images. The algorithm started from a preprocessing process, including image cropping, contrast enhancement, and noise filtering. The CNN then classified each image pixel into three categories: 1) enzyme active fluorescence microwell (or “On” microwell) 2) image defects and 3) background. The “On” microwells (Qred+) were segmented out as the output mask with defects removed. The architecture of the network was divided into a downsampling process for category classification and an upsampling process for pixel segmentation. The downsampling process was composed of 3 layers, including 2 convolution layers with a rectified linear unit, and a max-pooling layer in between. The upsampling process comprised a transposed convolution layer with ReLU, a softmax layer and a pixel classification layer. The bright-field images were then analyzed using Sobel edge detection method to detect empty/occupied wells to determine the overall beads filling rate. At last, the fraction of the Qred+ microwells with respect to the total bead-filled microwells (P_{on}) was calculated, and the Poisson’s distribution equation was used to calculate the mean expectation value: $\lambda = -\ln(1 - P_{on})$, which represented the average number of analyte–antibody immune complexes per bead and is proportional to the concentration of the analyte.

Statistics: All error bars presented in graphs are one standard deviation unless otherwise specified. Group analysis were all performed using an unpaired Welch’s *t* test and a *p*-value of <0.05 is considered as statistically significant. TNF- α measurements from primary microglia were also analyzed using a mixed-effects model. The effect of individual animals was modeled as a random effect, while genotype and exposure to LPS or A β were modeled as fixed effects. All fixed effects were coded as binary variables (0 for WT or absence of LPS and A β , 1 for 5xPAD or presence of LPS or A β) so that model estimates can be interpreted as the change in TNF- α due to the presence of the specified parameter. The model was executed in SPSS v27 (IBM).

Supporting Information

Supporting Information is available from the Wiley Online Library or from the author.

Acknowledgements

This research was supported by grants from the National Science Foundation CEBET 1931905 (K.K.) and the National Institute of Health K08NS101054 (B.H.S.). The authors also acknowledge technical support from staff at the University of Michigan Robert H. Lurie Nanofabrication Facility for device fabrication.

Conflict of Interest

The authors declare no conflict of interest.

Data Availability Statement

The data that support the findings of this study are available from the corresponding author upon reasonable request.

Keywords

Alzheimer's disease, amyloid-beta phagocytosis, cytokine secretion, digital immunoassay, microglia

Received: March 24, 2021

Revised: May 8, 2021

Published online: June 25, 2021

- [1] G. Arango Duque, A. Descoteaux, *Front. Immunol.* **2014**, *5*, 491.
- [2] J.-M. Zhang, J. An, *Int. Anesthesiol. Clin.* **2007**, *45*, 27.
- [3] C. Cao, M. Yu, Y. Chai, *Cell Death Dis.* **2019**, *10*, 782.
- [4] H. Chaudhry, J. Zhou, Y. Zhong, M. M. Ali, F. Mcguire, P. S. Nagarkatti, M. Nagarkatti, *In Vivo* **2013**, *27*, 669.
- [5] T. Rimmelé, D. Payen, V. Cantaluppi, J. Marshall, H. Gomez, A. Gomez, P. Murray, J. A. Kellum, *Shock* **2016**, *45*, 282.
- [6] J. M. Coghill, S. Sarantopoulos, T. P. Moran, W. J. Murphy, B. R. Blazar, J. S. Serody, *Blood* **2011**, *117*, 3268.
- [7] A. S. Henden, G. R. Hill, *J. Immunol.* **2015**, *194*, 4604.
- [8] D. W. Dickson, S. C. Lee, L. A. Mattiace, S.-H. C. Yen, C. Brosnan, *Glia* **1993**, *7*, 75.
- [9] J. A. Smith, A. Das, S. K. Ray, N. L. Banik, *Brain Res. Bull.* **2012**, *87*, 10.
- [10] W. Y. Wang, M. S. Tan, J. T. Yu, L. Tan, *Ann. Transl. Med.* **2015**, *3*, 136.
- [11] D. Finco, C. Grimaldi, M. Fort, M. Walker, A. Kiessling, B. Wolf, T. Salcedo, R. Faggioni, A. Schneider, A. Ibraghimov, S. Scesney, D. Serna, R. Prell, R. Stebbings, P. K. Narayanan, *Cytokine* **2014**, *66*, 143.
- [12] A. Rezk, R. Li, A. Bar-Or, *Sci. Rep.* **2020**, *10*, 14823.
- [13] K. Yang, X. J. Zhang, L. J. Cao, X. H. Liu, Z. H. Liu, X. Q. Wang, Q. J. Chen, L. Lu, W. F. Shen, Y. Liu, *PLoS One* **2014**, *9*, e95935.
- [14] J. Pan, J. Wan, *J. Immunol. Methods* **2020**, *486*, 112834.
- [15] R. W. Williams, *Mapping Genes that Modulate Mouse Brain Development: A Quantitative Genetic Approach*, Springer, Berlin Heidelberg **2000**, pp. 21–49.
- [16] V. Chokkalingam, J. Tel, F. Wimmers, X. Liu, S. Semenov, J. Thiele, C. G. Figdor, W. T. S. Huck, *Lab Chip* **2013**, *13*, 4740.
- [17] T. Konry, M. Dominguez-Villar, C. Baecher-Allan, D. A. Hafler, M. L. Yarmush, *Biosens. Bioelectron.* **2011**, *26*, 2707.
- [18] Y. Lu, J. J. Chen, L. Mu, Q. Xue, Y. Wu, P.-H. Wu, J. Li, A. O. Vortmeyer, K. Miller-Jensen, D. Wirtz, R. Fan, *Anal. Chem.* **2013**, *85*, 2548.
- [19] C. Ma, R. Fan, H. Ahmad, Q. H. Shi, B. Comin-Anduix, T. Chodon, R. C. Koya, C. C. Liu, G. A. Kwong, C. G. Radu, A. Ribas, J. R. Heath, *Nat. Med.* **2011**, *17*, 738.
- [20] Q. Shi, L. Qin, W. Wei, F. Geng, R. Fan, Y. Shik Shin, D. Guo, L. Hood, P. S. Mischel, J. R. Heath, *Proc. Natl. Acad. Sci. USA* **2012**, *109*, 419.
- [21] K. M. Summers, S. J. Bush, D. A. Hume, *PLoS Biol.* **2020**, *18*, e3000859.
- [22] A. Haque, P. Gheibi, Y. Gao, E. Foster, K. J. Son, J. You, G. Stybayeva, D. Patel, A. Revzin, *Sci. Rep.* **2016**, *6*, 33980.
- [23] Q. Hu, C. Luni, N. Elvassore, *Biochem. Biophys. Res. Commun.* **2018**, *497*, 480.
- [24] N. Jain, V. Vogel, *Nat. Mater.* **2018**, *17*, 1134.
- [25] Q. Xue, Y. Lu, M. R. Eisele, E. S. Sulistijo, N. Khan, R. Fan, K. Miller-Jensen, *Sci. Signaling* **2015**, *8*, ra59.
- [26] K. Bacon, A. Lavoie, B. M. Rao, M. Daniele, S. Menegatti, *Acta Biomater.* **2020**, *112*, 29.
- [27] J. Gust, K. A. Hay, L.-A. Hanafi, D. Li, D. Myerson, L. F. Gonzalez-Cuyar, C. Yeung, W. C. Liles, M. Wurfel, J. A. Lopez, J. Chen, D. Chung, S. Harju-Baker, T. Özpölat, K. R. Fink, S. R. Riddell, D. G. Maloney, C. J. Turtle, *Cancer Discovery* **2017**, *7*, 1404.
- [28] I. Lotan, F. Benninger, R. Mendel, M. A. Hellmann, I. Steiner, *Neurology: Neuroimmunol. Neuroinflammation* **2019**, *6*, e584.
- [29] *Lab. Anim.* **1993**, *27*, 1.
- [30] S. J. Denstaedt, J. L. Spencer-Segal, M. W. Newstead, K. Laborc, A. P. Zhao, A. Hjelmaas, X. Zeng, H. Akil, T. J. Standiford, B. H. Singer, *J. Immunol.* **2018**, *200*, 3188.
- [31] A. J. Kaestli, M. Junkin, S. Tay, *Lab Chip* **2017**, *17*, 4124.
- [32] R. Rodriguez-Moncayo, R. J. Jimenez-Valdes, A. M. Gonzalez-Suarez, J. L. Garcia-Cordero, *ACS Sens.* **2020**, *5*, 353.
- [33] A. Chen, T. Vu, G. Stybayeva, T. Pan, A. Revzin, *Biomicrofluidics* **2013**, *7*, 024105.
- [34] W. Chen, N.-T. Huang, B. Oh, R. H. W. Lam, R. Fan, T. T. Cornell, T. P. Shanley, K. Kurabayashi, J. Fu, *Adv. Healthcare Mater.* **2013**, *2*, 965.
- [35] B.-R. Oh, P. Chen, R. Nidetz, W. McHugh, J. Fu, T. P. Shanley, T. T. Cornell, K. Kurabayashi, *ACS Sens.* **2016**, *1*, 941.
- [36] B.-R. Oh, N.-T. Huang, W. Chen, J. H. Seo, P. Chen, T. T. Cornell, T. P. Shanley, J. Fu, K. Kurabayashi, *ACS Nano* **2014**, *8*, 2667.
- [37] A. Stephens, R. Nidetz, N. Mesyngier, M. T. Chung, Y. Song, J. Fu, K. Kurabayashi, *Lab Chip* **2019**, *19*, 3065.
- [38] T. Vu, A. Rahimian, G. Stybayeva, Y. Gao, T. Kwa, J. Van De Water, A. Revzin, *Biomicrofluidics* **2015**, *9*, 044115.
- [39] H. Zhu, G. Stybayeva, M. Macal, E. Ramanculov, M. D. George, S. Dandekar, A. Revzin, *Lab Chip* **2008**, *8*, 2197.
- [40] J. Zhu, J. He, M. Verano, A. T. Brimmo, A. Glia, M. A. Qasaimeh, P. Chen, J. O. Aleman, W. Chen, *Lab Chip* **2018**, *18*, 3550.
- [41] Y. Song, E. Sandford, Y. Tian, Q. Yin, A. G. Kozminski, S. H. Su, T. Cai, Y. Ye, M. T. Chung, R. Lindstrom, A. Goicochea, J. Barabas, M. Olesnavich, M. Rozwadowski, Y. Li, H. B. Alam, B. H. Singer, M. Ghosh, S. W. Choi, M. Tewari, K. Kurabayashi, *Blood* **2021**, *137*, 1591.
- [42] Y. Song, Y. Ye, S.-H. Su, A. Stephens, T. Cai, M.-T. Chung, M. K. Han, M. W. Newstead, L. Yessayan, D. Frame, H. D. Humes, B. H. Singer, K. Kurabayashi, *Lab Chip* **2021**, *21*, 331.
- [43] Y. Song, J. Zhao, T. Cai, A. Stephens, S.-H. Su, E. Sandford, C. Flora, B. H. Singer, M. Ghosh, S. W. Choi, M. Tewari, K. Kurabayashi, *Biosens. Bioelectron.* **2021**, *180*, 113088.
- [44] H. Oakley, S. L. Cole, S. Logan, E. Maus, P. Shao, J. Craft, A. Guillozet-Bongaarts, M. Ohno, J. Disterhoft, L. Van Eldik, R. Berry, R. Vassar, *J. Neurosci.* **2006**, *26*, 10129.
- [45] J. J. Muldoon, Y. Chuang, N. Bagheri, J. N. Leonard, *Nat. Commun.* **2020**, *11*, 878.
- [46] T. Bartels, S. De Schepper, S. Hong, *Science* **2020**, *370*, 66.
- [47] D. A. Galloway, A. E. M. Phillips, D. R. J. Owen, C. S. Moore, *Front. Immunol.* **2019**, *10*, 790.
- [48] J. P. Brás, J. Bravo, J. Freitas, M. A. Barbosa, S. G. Santos, T. Summavielle, M. I. Almeida, *Cell Death Dis.* **2020**, *11*, 415.
- [49] D. N. Doll, S. L. Rellick, T. L. Barr, X. Ren, J. W. Simpkins, *J. Neurochem.* **2015**, *132*, 443.
- [50] S. L. Yates, L. H. Burgess, J. Kocsis-Angle, J. M. Antal, M. D. Dority, P. B. Embury, A. M. Piotrkowski, K. R. Brunden, *J. Neurochem.* **2000**, *74*, 1017.
- [51] L. Ye, Y. Huang, L. Zhao, Y. Li, L. Sun, Y. Zhou, G. Qian, J. C. Zheng, *J. Neurochem.* **2013**, *125*, 897.
- [52] J. Cazareth, A. Guyon, C. Heurteaux, J. Chabry, A. Petit-Paitel, *J. Neuroinflammation* **2014**, *11*, 132.
- [53] W. J. Streit, H. Khoshbouei, I. Bechmann, *Glia* **2020**, *68*, 845.
- [54] K. A. Walker, B. N. Ficek, R. Westbrook, *ACS Chem. Neurosci.* **2019**, *10*, 3340.
- [55] A.-C. Wendeln, K. Degenhardt, L. Kaurani, M. Gertig, T. Ulas, G. Jain, J. Wagner, L. M. Häslér, K. Wild, A. Skodras, T. Blank, O. Staszewski, M. Datta, T. P. Centeno, V. Capece, M. R. Islam, C. Kerimoglu, M. Staufienbiel, J. L. Schultze, M. Beyer, M. Prinz, M. Jucker, A. Fischer, J. J. Neher, *Nature* **2018**, *556*, 332.
- [56] A. Shemer, D. Erny, S. Jung, M. Prinz, *Trends Immunol.* **2015**, *36*, 614.

- [57] M. Jana, C. A. Palencia, K. Pahan, *J. Immunol.* **2008**, *181*, 7254.
- [58] L. Meda, M. A. Cassatella, G. I. Szendrei, L. Otvos, P. Baron, M. Villalba, D. Ferrari, F. Rossi, *Nature* **1995**, *374*, 647.
- [59] X.-D. Pan, Y.-G. Zhu, N. Lin, J. Zhang, Q.-Y. Ye, H.-P. Huang, X.-C. Chen, *Mol. Neurodegener.* **2011**, *6*, 45.
- [60] S. Dudal, C. Morissette, D. Lacombe, P. Tremblay, F. Gervais, *J. Neuroimmunol.* **2004**, *153*, 26.
- [61] E. G. Njie, E. Boelen, F. R. Stassen, H. W. M. Steinbusch, D. R. Borchelt, W. J. Streit, *Neurobiol. Aging* **2012**, *33*, 195.e1.
- [62] R. M. Ransohoff, *Nat. Neurosci.* **2016**, *19*, 987.
- [63] E. B. Gökerküçük, M. Tramier, G. Bertolin, *Genes* **2020**, *11*, 125.
- [64] W. M. Partridge, *Front. Physiol.* **2020**, *11*, 398.
- [65] W. B. Varhue, L. Langman, M. Kelly-Goss, M. Lataillade, K. L. Brayman, S. Peirce-Cottler, N. S. Swami, *Lab Chip* **2017**, *17*, 3682.